

Cracking node method for dynamic fracture with finite elements

Jeong-Hoon Song[§] and Ted Belytschko^{*,†,‡}

Theoretical and Applied Mechanics, Northwestern University, Evanston, IL 60208-3111, U.S.A.

SUMMARY

A new method for modeling discrete cracks based on the extended finite element method is described. In the method, the growth of the actual crack is tracked and approximated with contiguous discrete crack segments that lie on finite element nodes and span only two adjacent elements. The method can deal with complicated fracture patterns because it needs no explicit representation of the topology of the actual crack path. A set of effective rules for injection of crack segments is presented so that fracture behavior beginning from arbitrary crack nucleations to macroscopic crack propagation is seamlessly modeled. The effectiveness of the method is demonstrated with several dynamic fracture problems that involve complicated crack patterns such as fragmentation and crack branching. Copyright © 2008 John Wiley & Sons, Ltd.

Received 12 May 2008; Accepted 23 May 2008

KEY WORDS: extended finite element method; discrete cohesive crack; dynamic fracture

1. INTRODUCTION

The ability to model discontinuities such as cracks, dislocations, and shear bands independently of the mesh topology is a very useful capability in a finite element method (FEM). The classical way to model discontinuities is to align the mesh so that the discontinuities are coincident with element edges and then to introduce an additional set of nodes so that the interpolation across the element edge is discontinuous. Such methods are called remeshing methods because the mesh must be changed to conform to the crack geometry at every time step. Examples are found in the works of Swenson and Ingraffea [1] and Martha *et al.* [2].

*Correspondence to: Ted Belytschko, Theoretical and Applied Mechanics, Northwestern University, Evanston, IL 60208-3111, U.S.A.

†E-mail: tedbelytschko@northwestern.edu

‡Walter P. Murphy and McCormick School Professor.

§Graduate Research Assistant.

Contract/grant sponsor: Office of Naval Research; contract/grant number: N00014-06-1-0380

However, these remeshing methods [1, 2] are quite unwieldy for modeling evolving discontinuities, especially dynamic crack growth, because they require remeshing and projections of field variables from the previous mesh. The time continuity of the solution is quite important in any numerical model, but, even with excellent projection schemes, significant errors in the velocities, stresses, and displacements can be introduced by remeshing. Furthermore, in most dynamic fracture problems, the crack advances over a large part of the mesh so that remeshing would need to be performed many times. Even when modeling stationary discontinuities, these methods can be quite cumbersome because the construction of a mesh that conforms to the surfaces of the discontinuities is often awkward.

One method that avoids these difficulties is the extended finite element method (XFEM) [3, 4], which introduces arbitrary discontinuities into the finite element approximation without mesh dependencies. The method is based on a partition of unity approach [5] but, in the XFEM, only a local partition of unity is used, i.e. the enrichment function spans only those element edges crossed by the discontinuity. The location of the discontinuity is usually defined by level set functions; see Stolarska *et al.* [6], Belytschko *et al.* [7], Ventura *et al.* [8, 9], and Prabel *et al.* [10]. The XFEM has been developed for three-dimensional fracture problems [11], two-dimensional fracture problems [12–14], and recently for shell fracture problems [15–17]. The method is also closely related to the *s*-version of the FEM [18], where a mesh with a crack is superimposed on the original mesh.

One major drawback of the XFEM is that complicated discontinuity patterns are difficult to resolve since the method is essentially a discontinuity tracking method; these difficulties are also found in shock tracking methods. For example, it is necessary to employ a crack branching algorithm to simulate crack branching [12, 14] since the method does not automatically follow multiple crack branches. This is exacerbated in treatments of crack growth with level sets since branching phenomena are not naturally treated within the original level set framework.

The purpose of the present study is to introduce a method that is a hybrid discontinuity tracking-fitting method. The basic idea is to fit discontinuities with a set of discrete discontinuities at nodes of the finite element mesh, which are oriented in the correct direction. One of the major advantage of this approach is that it can deal with complicated fracture patterns that appear to be beyond the capabilities of level set based discontinuity tracking methods. Many fracture problems are of this type: fragmentation problems and problems that involve the growth and branching of multiple cracks. However, the placement and the sharpness of the discontinuity representation may be diminished because the discrete discontinuities are centered at the nodes. Nevertheless, we show that these types of problems can be handled effectively by this method by several representative examples. The method is especially well suited to explicit finite element procedures [19].

The proposed method is an outgrowth of a large number of different types of methods for modeling crack growth. We cannot review the entire literature here, but only summarize some of the key works on the major methods. In addition to remeshing methods, the methods for crack modeling can be classified in four groups:

- (1) element interface discontinuity methods [20, 21] often called ‘cohesive zone methods’; however, the latter name is ambiguous because cohesive zones can be used with other numerical methods for fracture;
- (2) embedded discontinuity methods [22] often called the ‘strong discontinuity methods’, (the latter is a misleading term since many of the other methods, such as XFEM and element interface discontinuity methods in fact model cleaner strong discontinuities);

- (3) element deletion methods, often called the ‘element erosion methods’;
- (4) enrichment methods, such as XFEM [3, 4], and the generalized FEM [23–25].

Element interface discontinuity methods employ discontinuity models that are identical to those in remeshing methods, i.e. element edges are coincident with the discontinuity and both surfaces of the discontinuity have independent element edges and nodes. No effort is needed to track the discontinuity with remeshing. These methods rely on dense meshes to approximately capture the topology of the discontinuity and on cohesive surfaces to model the nucleation and evolution of the discontinuity. Two forms have evolved: methods where separation of element edges is possible on all element edges from the beginning of the simulation as in Xu and Needleman [20] and methods where the cohesive surfaces are injected selectively along the cracked elements edges, as developed by Camacho and Ortiz [21] and Ortiz and Pandolfi [26]. In the former, errors are introduced in the bulk properties of the material and convergence is not clear. Papoulia *et al.* [27, 28] have also pointed out that errors occur due to the lack of continuity when cohesive laws are injected; this issue must also be considered in the use of XFEM with cohesive traction laws. Overall, these methods show a significant degree of mesh sensitivity [12, 29], although Zavattieri and Espinosa [30] and Zhou and Molinari [31] have shown that introducing a degree of randomness in the cohesive strength ameliorates this problem.

Embedded discontinuity methods employ discontinuities in elements based on incompatible fields. They are equivalent to introducing a band of high deformation, as introduced in Belytschko *et al.* [22]. A key improvement was made by Dvorkin *et al.* [32], who introduced a kinematic method to suppress locking of these methods. There has been an extensive literature on this method; as examples we cite Simo *et al.* [33] and Armero and Garikipati [34]. An excellent review is given by Jirásek [35].

Element deletion methods are one of the simplest methods to implement. The attractiveness of the method lies in the fact that it requires no alteration of standard finite element software. The crack is modeled through the constitutive equations in which the stress vanishes at specified criteria. Because of their simplicity, these methods have been widely used in industry; they are perhaps the most widely used. In these methods, it is imperative that the constitutive equation be adjusted with respect to the element size so that the fracture energy is independent of the element size. However, even with these modifications to the constitutive equations, the element deletion method suffers from substantial mesh dependencies. It was shown that the element deletion method completely fails in the prediction of crack branching for structured meshes in Song *et al.* [29]. These methods have recently been studied by Fan and Fish [36], who report rather good results when element volume corrections are made to the constitutive equations.

In enrichment methods, such as XFEM [3, 4], the discontinuity is completely independent of the mesh topology, and the results for different meshes of the same refinement yield almost identical crack paths. The major difficulty in their implementation is that the methods are based on a continuous crack path. This complicates the programming of these methods for situations where extensive cracking, crack joining, and crack branching take place.

The proposed method is aimed at alleviating this disadvantage, albeit at some cost in accuracy and fidelity in tracking the actual crack paths. The method is closely related to the XFEM; the major difference is in the morphology of the discontinuities, i.e. it introduces discontinuous fields only at the nodes.

A similar approach was introduced by Remmers *et al.* [37] and de Borst *et al.* [38]. The major difference of the described method from that of Remmers *et al.* [37] is that each crack spans

only two elements adjacent to the cracked node whereas in [37], the segments are identified with elements and span three elements. Our approach simplifies the implementation and also seems to improve the results for crack speeds. We have also introduced rules and procedures into the algorithm that appear to be essential for dynamic fracture. The described method has also been pursued in meshless methods under the cognomen ‘*cracking particle methods*’ by Rabczuk and Belytschko [39], Rabczuk *et al.* [40], and Rabczuk and Samaniego [41].

2. GOVERNING EQUATIONS

The method is in principle applicable to two or three dimensions, but henceforth we describe it only for the two-dimensional case. Consider an initial domain $\Omega_0 \in \mathbb{R}^2$ and its boundary Γ^0 as shown in Figure 1; $\Gamma_t^0 \cup \Gamma_v^0 = \Gamma^0$ and $\Gamma_t^0 \cap \Gamma_v^0 = \emptyset$. We allow this domain to contain internal discontinuities Γ_c^0 . Let $\tilde{\Omega}_0$ be the open set, which excludes all discontinuities, i.e. $\tilde{\Omega}_0 = \Omega_0 \setminus \Gamma_c^0$. In the current domain, the images of the initial domain Ω_0 and $\tilde{\Omega}_0$ are denoted by Ω and $\tilde{\Omega}$, respectively, and the motion is described by $\mathbf{x} = \boldsymbol{\phi}(\mathbf{X}, t)$, where t is the time, and \mathbf{X} and \mathbf{x} are material and spatial co-ordinates, respectively. In the motion, the displacement at the material point \mathbf{X} is denoted by $\mathbf{u}(\mathbf{X}, t)$.

The strong form of the linear momentum equation in the current configuration Ω can easily be developed by changing the kinetic and kinematic quantities of the strong form in the reference configuration Ω_0 ; see Belytschko *et al.* [42] for a text-book account. The strong form of the linear momentum equation in the updated Lagrangian description is given by

$$\frac{\partial \sigma_{ji}}{\partial x_j} + \rho b_i = \rho \ddot{u}_i \quad \text{in } \tilde{\Omega} \tag{1}$$

in conjunction with the boundary conditions:

$$n_j \sigma_{ji} = \bar{t}_i \quad \text{on } \Gamma_t \tag{2}$$

$$v_i = \bar{v}_i \quad \text{on } \Gamma_v \tag{3}$$

$$n_j^+ \sigma_{ji}^+ = n_k^- \sigma_{ki}^- = t_i^c \quad \text{on } \Gamma_c \tag{4}$$

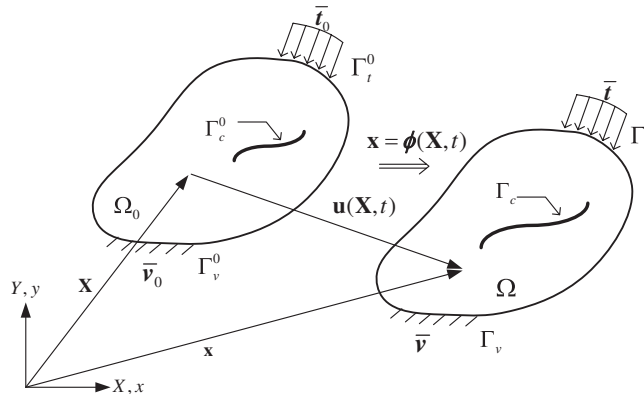


Figure 1. A two-dimensional body with a discontinuity and its representation in the reference and the current domains.

where $\boldsymbol{\sigma}$ is the Cauchy stress, ρ is the current density, \mathbf{b} is the body force, \mathbf{n}^+ and \mathbf{n}^- are the normals to the relevant surfaces in the current configuration, and \mathbf{t}^c is the cohesive traction along the crack surfaces. Equation (4) represents the cohesive traction condition.

3. REPRESENTATION OF CRACK BY CRACKING NODES

In this method, the actual crack path is approximated by a set of discrete crack segments that are restricted to pass through the nodes of the finite element mesh. Henceforth, we will refer to nodes that are crossed by the discrete crack segments as *cracked nodes*. A typical arrangement of cracked nodes is shown in Figure 2 along with the actual crack path that is approximated. It can be seen that the cracked node method approximates the actual crack path by a set of discrete crack segments and an explicit representation of the continuous actual crack path is unnecessary. It is only necessary to construct and keep track of a list of cracked nodes. This feature enables the method to avoid the complexity of level set methods for tracking crack geometry.

Let the set of all finite element nodes be \mathcal{S} and the set of cracked nodes be \mathcal{S}_c ; hence, $\mathcal{S}_c \subset \mathcal{S}$ and $\mathcal{S}_c \cap \mathcal{S} = \mathcal{S}_c$. When a crack segment is injected at node I , the normal to the crack surface \mathbf{n}_I^{ter} must be defined with respect to the crack injection time t_{cr} ; the normal to the crack is defined by a fracture criterion that will be discussed later. Once a crack is injected at the node, the normal is fixed in the material coordinate system. Thus, the crack will rotate with the material in time. The displacement approximation is given by the XFEM approach [4]:

$$\begin{aligned} \mathbf{u}(\mathbf{X}, t) &= \mathbf{u}^{\text{cont}}(\mathbf{X}, t) + \mathbf{u}^{\text{disc}}(\mathbf{X}, t) \\ &= \sum_{I \in \mathcal{S}} N_I(\mathbf{X}) \mathbf{u}_I(t) + \sum_{J \in \mathcal{S}_c} N_J(\mathbf{X}) H(\zeta_J(\mathbf{X})) \mathbf{q}_J(t) \end{aligned} \quad (5)$$

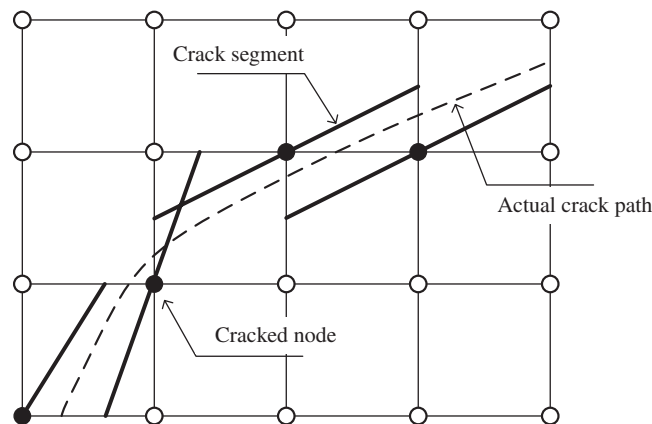


Figure 2. Schematic of a typical arrangement of cracked nodes: hollow and solid circles denote regular and cracked nodes, respectively, and the dashed line represents the actual crack path.

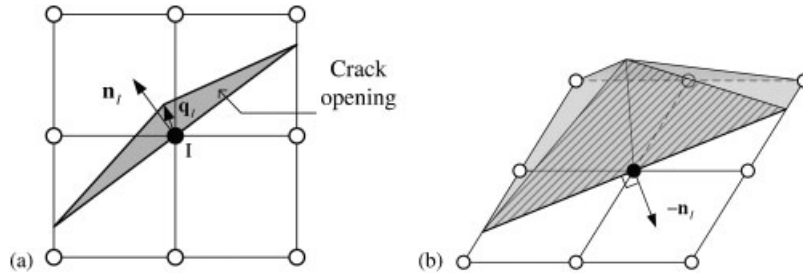


Figure 3. Schematic of crack opening at cracked node I and its enriched finite element nodal shape function: \mathbf{n}_I is the normal to crack surface and \mathbf{q}_I denotes extra degrees of freedom that determine the crack opening.

where $\mathbf{u}^{\text{cont}}(\mathbf{X}, t)$ and $\mathbf{u}^{\text{disc}}(\mathbf{X}, t)$ denote continuous and discontinuous displacement fields, respectively, and $\zeta_J(\mathbf{X})$ defines the crack geometry by

$$\zeta_J(\mathbf{X}) = \mathbf{n}_J^0 \cdot \frac{\mathbf{X} - \mathbf{X}_J}{\|\mathbf{X} - \mathbf{X}_J\|} \tag{6}$$

and $H(\cdot)$ is the Heaviside step function:

$$H(x) = \begin{cases} 1 & \forall x \geq 0 \\ 0 & \forall x < 0 \end{cases} \tag{7}$$

Note that in the definition of $\zeta_J(\mathbf{X})$ in Equation (6), \mathbf{n}^0 is the normal to the crack surface in the reference configuration Ω_0 ; when a crack is injected at node I with normal $\mathbf{n}_I^{t_{\text{cr}}}$, it must be pulled back to the reference configuration Ω_0 by Nanson's law:

$$\mathbf{n}_I^0 = J^{-1} \mathbf{n}_I^{t_{\text{cr}}} \cdot \mathbf{F}(\mathbf{X}_I, t_{\text{cr}}) \tag{8}$$

where \mathbf{F} is the deformation gradient tensor at the material point \mathbf{X} at time t_{cr} and J is the determinant of the deformation gradient tensor. The crack opening of each discrete crack segment is a wedge function as shown in Figure 3(a). We do not account for the change in angle between the normal and the crack surface that can occur due to large shear strains. This can easily be accounted for by defining the crack surface in terms of the material or element coordinates.

The velocity is given by the material time derivative of the displacement approximation (Equation (5)):

$$\mathbf{v}(\mathbf{X}, t) = \sum_{I \in \mathcal{S}} N_I(\mathbf{X}) \dot{\mathbf{u}}_I(t) + \sum_{J \in \mathcal{S}_c} N_J(\mathbf{X}) H(\zeta_J(\mathbf{X})) \dot{\mathbf{q}}_J(t) \tag{9}$$

where superposed dots denote material time derivatives. The components of the spatial gradient of the velocity, $\nabla \mathbf{v} (= \mathbf{L})$, are given by

$$v_{i,j} = L_{ij} = \sum_{I \in \mathcal{S}} N_{I,j}(\mathbf{X}) \dot{u}_{iI}(t) + \sum_{J \in \mathcal{S}_c} N_{J,j}(\mathbf{X}) H(\zeta_J(\mathbf{X})) \dot{q}_{iJ}(t) \tag{10}$$

where a subscript comma denotes differentiation with respect to the spatial coordinates. The derivatives of the shape function are taken with respect to the spatial variables, but this causes no

difficulties since the shape functions are generally expressed in terms of parent element coordinates and implicit differentiation must be used whether the derivatives are with respect to the spatial or material coordinates.

4. WEAK FORM AND DISCRETIZATION

The weak form (principal of virtual power) of the updated Lagrangian description is given as follows: find $v_i \in \mathcal{V}$ such that

$$\delta \mathcal{P}^{\text{kin}} = \delta \mathcal{P}^{\text{ext}} - \delta \mathcal{P}^{\text{int}} + \delta \mathcal{P}^{\text{coh}} \quad \forall \delta v_i \in \mathcal{V}_0 \quad (11)$$

where

$$\delta \mathcal{P}^{\text{kin}} = \int_{\tilde{\Omega}} \delta v_i \rho \dot{v}_i \, d\tilde{\Omega} \quad (12)$$

$$\delta \mathcal{P}^{\text{int}} = \int_{\tilde{\Omega}} \delta D_{ij} \sigma_{ij} \, d\tilde{\Omega} = \int_{\tilde{\Omega}} \frac{\partial(\delta v_i)}{\partial x_j} \sigma_{ij} \, d\tilde{\Omega} \quad (13)$$

$$\delta \mathcal{P}^{\text{ext}} = \int_{\Gamma_t} \delta v_i \bar{t}_i \, d\Gamma + \int_{\tilde{\Omega}} \delta v_i \rho b_i \, d\tilde{\Omega} \quad (14)$$

$$\delta \mathcal{P}^{\text{coh}} = \int_{\Gamma_c} \llbracket \delta v_i \rrbracket n_i t^c \, d\Gamma \quad (15)$$

where $\delta \mathcal{P}^{\text{kin}}$ is the kinetic power, $\delta \mathcal{P}^{\text{ext}}$ is the external power, $\delta \mathcal{P}^{\text{int}}$ is the internal power, $\delta \mathcal{P}^{\text{coh}}$ is the power of the cohesive traction across the crack surface Γ_c with the cohesive traction t^c , and $\llbracket \cdot \rrbracket$ denotes a jump in the function. Standard indicial notation with repeated indices implying summation is used.

The admissible spaces for the velocity fields are defined as follows:

$$\mathcal{V} = \{v_i | v_i \in \mathcal{H}^1 \text{ in } \tilde{\Omega}, v_i = \bar{v}_i \text{ on } \Gamma_v, \text{ and discontinuous on } \Gamma_c\} \quad (16)$$

$$\mathcal{V}_0 = \{\delta v_i | \delta v_i \in \mathcal{H}^1 \text{ in } \tilde{\Omega}, \delta v_i = 0 \text{ on } \Gamma_v \cup \Gamma_c\} \quad (17)$$

The discrete equations are constructed by the standard Galerkin procedure from Equation (11) with the trial functions (Equation (9)). The test functions are of identical form:

$$\delta \mathbf{v}(\mathbf{X}, t) = \sum_{I \in \mathcal{I}} N_I(\mathbf{X}) \delta \dot{\mathbf{u}}_I(t) + \sum_{J \in \mathcal{J}_c} N_J(\mathbf{X}) H(\zeta_J(\mathbf{X})) \delta \dot{\mathbf{q}}_J(t) \quad (18)$$

The discrete momentum equations are

$$M_{ijIJ} \dot{v}_{jJ} = f_{iI}^{\text{ext}} - f_{iI}^{\text{int}} + f_{iI}^{\text{coh}} \quad (19)$$

where uppercase subscripts denote nodes and lowercase indices refer to components. The mass matrix is given by

$$\mathbf{M}_{IJ} = \begin{bmatrix} \mathbf{M}_{IJ}^{uu} & \mathbf{M}_{IJ}^{uq} \\ (\mathbf{M}_{IJ}^{uq})^T & \mathbf{M}_{IJ}^{qq} \end{bmatrix} \quad (20)$$

and the remaining terms are defined below:

$$\mathbf{v}_I = \begin{Bmatrix} \dot{\mathbf{u}}_I \\ \dot{\mathbf{q}}_I \end{Bmatrix}, \quad \mathbf{f}_I^{\text{int}} = \begin{Bmatrix} \mathbf{f}_I^{u,\text{int}} \\ \mathbf{f}_I^{q,\text{int}} \end{Bmatrix} \quad (21)$$

$$\mathbf{f}_I^{\text{ext}} = \begin{Bmatrix} \mathbf{f}_I^{u,\text{ext}} \\ \mathbf{f}_I^{q,\text{ext}} \end{Bmatrix}, \quad \mathbf{f}_I^{\text{coh}} = \begin{Bmatrix} \mathbf{0} \\ \mathbf{f}_I^{q,\text{coh}} \end{Bmatrix} \quad (22)$$

where

$$\mathbf{M}_{ijIJ}^{uu} = \delta_{ij} \int_{\tilde{\Omega}_0} \rho_0 N_I N_J \, d\Omega_0 \quad \forall I, J \in \mathcal{S} \quad (23)$$

$$\mathbf{M}_{ijIJ}^{uq} = \delta_{ij} \int_{\tilde{\Omega}_0} \rho_0 N_I N_J H(\zeta_J(\mathbf{X})) \, d\Omega_0 \quad \forall I \in \mathcal{S}, J \in \mathcal{S}_c \text{ or } \forall J \in \mathcal{S}, I \in \mathcal{S}_c \quad (24)$$

$$\mathbf{M}_{ijIJ}^{qq} = \delta_{ij} \int_{\tilde{\Omega}_0} \rho_0 N_I N_J H(\zeta_I(\mathbf{X})) H(\zeta_J(\mathbf{X})) \, d\Omega_0 \quad \forall I, J \in \mathcal{S}_c \quad (25)$$

$$\mathbf{f}_{iI}^{u,\text{int}} = \int_{\tilde{\Omega}} N_{I,j} \sigma_{ji} \, d\Omega \quad \forall I \in \mathcal{S} \quad (26)$$

$$\mathbf{f}_{iI}^{q,\text{int}} = \int_{\tilde{\Omega}} N_{I,j} H(\zeta_I(\mathbf{x})) \sigma_{ji} \, d\Omega \quad \forall I \in \mathcal{S}_c \quad (27)$$

$$\mathbf{f}_{iI}^{u,\text{ext}} = \int_{\Gamma_t} N_I \bar{t}_i \, d\Gamma + \int_{\Omega} N_I b_i \, d\Omega \quad \forall I \in \mathcal{S} \quad (28)$$

$$\mathbf{f}_{iI}^{q,\text{ext}} = \int_{\Gamma_t} N_I H(\zeta_I(\mathbf{x})) \bar{t}_i \, d\Gamma + \int_{\tilde{\Omega}} N_I H(\zeta_I(\mathbf{x})) b_i \, d\Omega \quad \forall I \in \mathcal{S}_c \quad (29)$$

$$\mathbf{f}_{iI}^{q,\text{coh}} = 2 \int_{\Gamma^c} N_I n_i t^c \, d\Gamma \quad \forall I \in \mathcal{S}_c \quad (30)$$

Note that in Equations (23)–(25), the components of the mass matrix \mathbf{M} have been expressed in the reference configuration to emphasize that it is time invariant. Also note that the cohesive forces across the crack only yield nodal forces corresponding to the degrees of freedom associated with \mathbf{q}_I .

5. IMPLEMENTATION

The proposed cracking node method can easily be embedded within a standard explicit dynamic finite element code by adding extra degrees of freedom to nodes as they crack. Henceforth, we concentrate on describing the numerical implementation within an explicit dynamic finite element code with four-node quadrilateral elements with one-point quadrature [43]. These elements are

widely used for explicit dynamic simulation and in the same spirit as the cracking node method: fast and efficient, but require fine meshes for accuracy. The methodology is feasible with other elements in two or three dimensions, but we do not discuss implementations for these elements here.

5.1. Computation of element internal forces using the averaged strain

The major consideration in the implementation of the cracking node method is developing an efficient procedure for the numerical integration of the nodal forces (Equations (26)–(27)) over the elements that contain cracked nodes. In this study, we adopted the one-point quadrature scheme along with the averaging procedure developed in Flanagan and Belytschko [43]. The averaged rate of deformation for element e , $\bar{\mathbf{D}}^e$, is defined in terms of the averaged velocity gradient $\nabla \bar{\mathbf{v}}^e$ by

$$\bar{\mathbf{D}}_{ij}^e = \frac{1}{2}(\bar{v}_{i,j}^e + \bar{v}_{j,i}^e) \quad (31)$$

where

$$\nabla \bar{\mathbf{v}}^e = \bar{v}_{i,j}^e = \frac{1}{A^e} \int_{\bar{\Omega}^e} v_{i,j} \, d\Omega \quad (32)$$

where A^e is the area of element e . Substituting Equation (10) into (32) and expressing the integrand in terms of parent element coordinates ξ gives

$$\bar{v}_{i,j}^e = \frac{1}{A^e} \int_{\bar{\Omega}^e} \left\{ \sum_{I \in \mathcal{S}} N_{I,j}(\xi) \dot{u}_{iI}(t) + \sum_{J \in \mathcal{S}_c} N_{J,j}(\xi) H(\zeta_J(\xi)) \dot{q}_{iJ}(t) \right\} d\Omega \quad (33)$$

Note that the arguments \mathbf{X} in Equation (10) are usually expressed in terms of parent element coordinates ξ by an isoparametric mapping in standard finite element codes.

In Flanagan and Belytschko [43], it is shown that for a four-node quadrilateral element

$$\int_{\Omega^e} N_{I,i}(\xi) \, d\Omega = A^e N_{I,i}(\mathbf{0}) \quad (34)$$

For elements with cracked nodes we make the approximation that

$$\int_{\Omega^e} N_{I,i}(\xi) H(\zeta_I(\xi)) \, d\Omega = A_I^e N_{I,i}(\mathbf{0}) \quad (35)$$

where

$$A_I^e = \int_{\Omega^e} H(\zeta_I(\xi)) \, d\Omega \quad (36)$$

The area A_I^e is the fractional area of the portion of element e on the nonzero side of the step function, i.e. where $H(\zeta_I) > 0$ as illustrated in Figure 4(a). Note that A_I^e is nonzero only for elements that include node I . Consider the generic elements e_1 – e_4 that contain two cracked nodes 1 and 2, as shown in Figure 4(b). $A_1^{e_1}$ has the same area as element e_1 , i.e. $A_1^{e_1} = A^{e_1}$ since $H(\zeta_1(\mathbf{X})) > 0$ in the entire element e_1 ; $A_2^{e_1}$ is the fractional area to the left of the crack Γ_{c2} since $\zeta_2(\mathbf{X}) < 0$ to the right of Γ_{c2} .

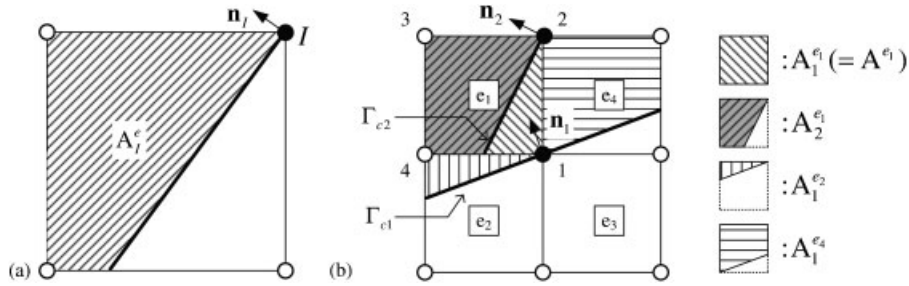


Figure 4. Areas A_I^e for (a) cracked node I and (b) generic elements e_1 – e_4 and cracked nodes 1 and 2.

Substituting Equations (34)–(36) into (33) gives the spatial gradient of the averaged velocity, $\bar{v}_{i,j}^e(\mathbf{0})$, for element e :

$$\bar{v}_{i,j}^e(\mathbf{0}) = \sum_{I=1}^4 N_{I,j}(\mathbf{0}) \dot{u}_{iI} + \frac{1}{A^e} \sum_{J=1}^{n_{cr}^e} A_J^e N_{J,j}(\mathbf{0}) \dot{q}_{iJ} \quad (37)$$

where n_{cr}^e is the number of cracked nodes in the element e and the argument of the shape functions is the origin of the parent element domain.

The averaged stress rate at the quadrature point is given by

$$\bar{\sigma}_{ij}^{e\nabla} = \mathcal{C}_{ijkl} \bar{D}_{kl}^e + \text{rotation terms} \quad (38)$$

where $\bar{\sigma}^{e\nabla}$ is the averaged frame invariant rate of Cauchy stress of element e and \mathcal{C} is the tangent modulus.

The nodal internal forces are also evaluated by the procedure given in Flanagan and Belytschko [43]. The nodal internal forces corresponding to the regular degrees of freedom for element e are

$$\begin{aligned} f_{iI(e)}^{u,int} &= \int_{\tilde{\Omega}^e} N_{I,j}(\xi) \bar{\sigma}_{ji}^e(\xi) d\Omega \quad \forall I \in \mathcal{S} \\ &\simeq A^e N_{I,j}(\mathbf{0}) \bar{\sigma}_{ji}^e(\mathbf{0}) + f_{iI(e)}^{stb} \end{aligned} \quad (39)$$

where $f_{iI(e)}^{stb}$ denotes the hourglass stabilization forces that are needed because of one-point integration; the hourglass control method from Flanagan and Belytschko [43] with critical damping as described in Daniel and Belytschko [44] is used. Similarly, the nodal internal forces related to the enriched degrees of freedom are

$$\begin{aligned} f_{iI(e)}^{q,int} &= \int_{\tilde{\Omega}^e} N_{I,j}(\xi) H(\zeta_I(\xi)) \bar{\sigma}_{ji}^e(\xi) d\Omega^e \quad \forall I \in \mathcal{S}_c \\ &\simeq A_I^e N_{I,j}(\mathbf{0}) \bar{\sigma}_{ji}^e(\mathbf{0}) + f_{iI(e)}^{stb} \\ &= \frac{A_I^e}{A^e} f_{iI(e)}^{u,int} \end{aligned} \quad (40)$$

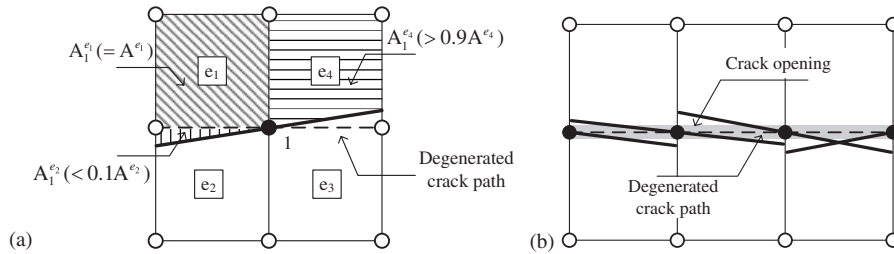


Figure 5. Degeneration of the cracked node method to the element interface discontinuity method: dashed line represents the line of degenerated interface discontinuities.

When a crack is nearly coincident with an edge as shown in Figure 5(a), the fractional area A_I^e is modified as follows so that the crack is aligned with the element edge:

$$A_I^e = \begin{cases} 0 & \text{if } A_I^e < 0.1A^e \\ A^e & \text{if } A_I^e > 0.9A^e \end{cases} \quad (41)$$

In the case, the proposed method degenerates to the element interface discontinuity method [20, 21, 26] and provides a discontinuity that is coincident with the element edge as shown in Figure 5(b).

5.2. Computation of lumped mass matrix for cracked elements

In the explicit dynamic method, a computation of nodal accelerations, which are the primary unknowns, is accomplished without implicitly solving any equations by using a diagonalized mass matrix, i.e. lumped mass matrix: it is one of the distinct characteristics of the explicit dynamic method.

However, when we employ XFEM [3, 4] within the framework of the explicit dynamic method, a construction of the lumped diagonal mass entails the following difficulties:

- (1) the lumped mass for the enriched degrees of freedom can be negative, which is unphysical;
- (2) the critical time step depends on the location of the crack, i.e. the critical time step is largest when the discontinuity is located at the center of the element and decreases to zero as the discontinuity is moved toward an element edge or node [14].

Several methods have been proposed to circumvent these difficulties: implicit (in cracked elements)–explicit (in continuum elements) time integration [12] and modified mass lumping schemes [39, 45, 46].

In the computations reported here, the mass for regular degrees of freedom, $\mathbf{M}^{uu, \text{lump}}$, is diagonalized by the conventional row sum technique:

$$\mathbf{M}_I^{uu, \text{lump}} = \sum_J \mathbf{M}_{IJ}^{uu} \quad \forall I, J \in \mathcal{S} \quad (42)$$

where \mathbf{M}_{IJ}^{uu} is the consistent mass matrix, which is defined by Equation (23). However, the lumped mass for the enriched degrees of freedoms, $\mathbf{M}^{qq, \text{lump}}$, is constructed by a diagonalization technique

based on the area fractions:

$$\mathbf{M}_I^{qq,lump} = \sum_e \frac{A_I^e}{A^e} \mathbf{M}_I^{uu,lump} \quad \forall I \in \mathcal{S}_c \quad (43)$$

where e denotes the adjacent elements of cracked node I . The diagonalized mass for the whole system is then given by

$$\mathbf{M}^{lump} = \begin{Bmatrix} \mathbf{M}^{uu,lump} \\ \mathbf{M}^{qq,lump} \end{Bmatrix} \quad (44)$$

6. CRACK LAW

6.1. Fracture criterion and cohesive model

The application of this method requires a criterion for crack nucleation along with a crack propagation law. Since we have focused on quasi-brittle fracture, we have used a maximum principal tensile strain criterion for the nucleation of cracks. The criterion is applied to a smoothed C^0 strain field, which is computed by a moving least square approximation; smoothing reduces spurious crack nucleation. When a measure of maximum principal tensile strain at a node exceeds the crack nucleation criterion, a crack segment is injected at that node with a normal so that the crack surface is coincident with the maximum principal tensile plane. The nucleation criterion is also used as a crack propagation criterion.

A cohesive crack model is prescribed along newly injected crack surfaces until the crack opening is fully developed, i.e. until the cohesive traction has vanished. In this study, we prescribed only the normal traction for the linear cohesive model since crack propagation is usually due to mode I fracture behavior in quasi-brittle materials. A penalty force was added to prevent crack surface overlap as shown in Figure 6.

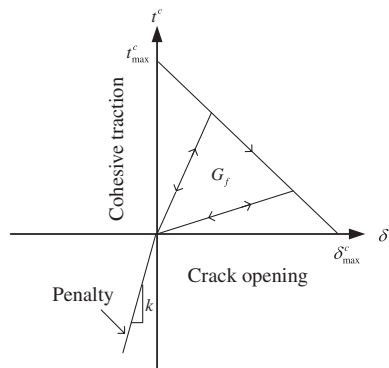


Figure 6. Schematic of a linear cohesive law: the area under the curve is the fracture energy, G_f .

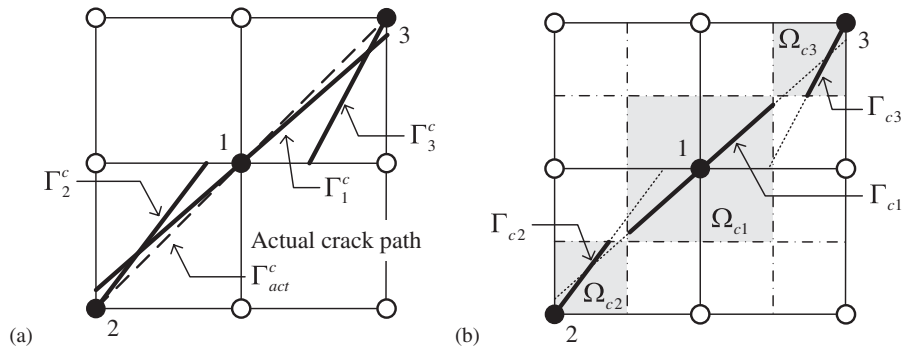


Figure 7. Schematic of the integration domain of the cohesive law along with the crack segments: (a) the integration domain of the cohesive law without modification and (b) the modified integration domain with improved fitting to the actual cohesive energy.

The cohesive model is constructed so that the dissipated energy due to the crack nucleation is equivalent to the fracture energy:

$$G_f = \int_0^{\delta_{\max}^c} t^c(\delta^c) d\delta = \frac{1}{2} t_{\max}^c \delta_{\max}^c \quad (45)$$

where δ_{\max}^c is the maximum normal crack opening displacement, G_f is the fracture energy, and δ^c is the jump in the displacement normal to the crack surface Γ_c , which is given by

$$\begin{aligned} \delta^c &= \frac{1}{2} \mathbf{n}^0 \cdot [\mathbf{u}(\mathbf{X}, t)]_{\mathbf{X} \in \Gamma_c^0} \\ &= \frac{1}{2} \sum_{I \in \mathcal{I}_c} \mathbf{n}^0 \cdot \mathbf{q}_I N_I(\mathbf{X})|_{\mathbf{X} \in \Gamma_c^0} \end{aligned} \quad (46)$$

For a material, G_f is given; t_{\max}^c is the traction computed at failure. The value of δ_{\max}^c is computed from Equation (45) based on G_f and t_{\max}^c . Note that the cohesive strength t_{\max}^c is not a constant parameter in this method. Unless t_{\max}^c takes on the current value of the traction when a crack segment is injected into a continuum finite element, the cohesive traction does not satisfy time continuity and may lead to severe noise; see Papoulia *et al.* [27]. We compute the cohesive strength t_{\max}^c with a moving least square scheme.

The cracking node method requires a modification of the cohesive forces for adjacent cracked nodes; otherwise, the cohesive energy is overpredicted. Consider a typical cracking pattern shown in Figure 7(a). Let Γ_{act}^c be the actual crack path, i.e. the continuous crack path, and model it by discrete crack segments Γ_1^c , Γ_2^c , and Γ_3^c . When all of the actual crack has opened so that

$$\delta^c(\mathbf{X}) > \delta_{\max}^c \quad \forall \mathbf{X} \in \Gamma_{\text{act}} \quad (47)$$

then the total cohesive energy dissipated by fracture along the actual crack path is given by

$$\begin{aligned} \mathcal{W}_{\text{act}}^{\text{coh}} &= \int_{\Gamma_{\text{act}}^c} \int_0^{\delta_{\max}^c} t^c(\delta^c) d\delta d\Gamma \\ &= G_f J_{\text{act}}^c \end{aligned} \quad (48)$$

where l_{act}^c is the length of actual crack Γ_{act}^c . The total cohesive energy due to the cohesive traction along the set of crack segments $\Gamma_1^c, \Gamma_2^c,$ and Γ_3^c is given by

$$\begin{aligned} \mathcal{W}^{coh} &= \sum_{I=1}^3 \int_{\Gamma_I^c} \int_0^{\delta_{max}^c} t^c(\delta^c) d\delta d\Gamma \\ &= G_f \sum_{I=1}^3 l_I^c \\ &\cong G_f 2l_{act}^c = 2\mathcal{W}_{act}^{coh} \end{aligned} \tag{49}$$

where $\sum l_I^c \cong 2l_{act}^c$ is used for the last equality, which is apparent from Figure 7(a). As we can see from Equation (49), unless we modify the integration domains of these cohesive crack segments, the total cohesive energy will substantially exceed the actual cohesive energy.

For this reason, we compute the cohesive forces based on Voronoi cells Ω_{cI} as shown in Figure 7(b). In this scheme, we activate the cohesive forces only on a single segment Γ_{cI} within a Voronoi cell Ω_{cI} . This modification gives a good approximation of the actual energy dissipation since $\sum_I l_{cI} \cong l_{act}^c$.

6.2. Crack initiation and propagation law

The cracking node method requires a set of effective rules for injection of crack segments so that fracture behavior, beginning from arbitrary crack nucleations to macroscopic crack propagation is seamlessly modeled. If a crack segment is injected at any node without any restriction, spurious crack patterns such as that shown in Figure 8(a) can develop. Such distributions of cracking nodes are quite meaningless since they imply a crack spacing equivalent to the resolution of the finite element model. It is obviously inappropriate to model fracture behavior that is not consistent with the resolution of the finite element mesh. These spurious crack patterns are prevented in the cracking node method by a set of crack injection rules that lead to more realistic crack patterns such as shown in Figure 8(b).

A simple rule, such as prohibiting further cracking around already cracked nodes, is a tempting way to prevent spread of parallel cracks. However, it also prevents important dynamic fracture

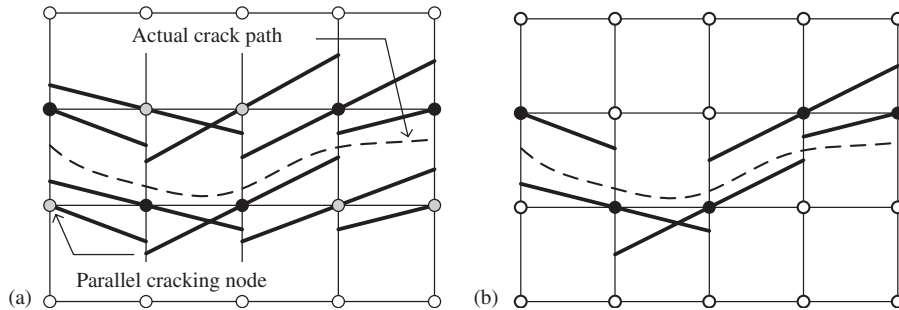


Figure 8. Schematic of cracking node patterns: (a) an unrealistic pattern and (b) an improved cracked node pattern.

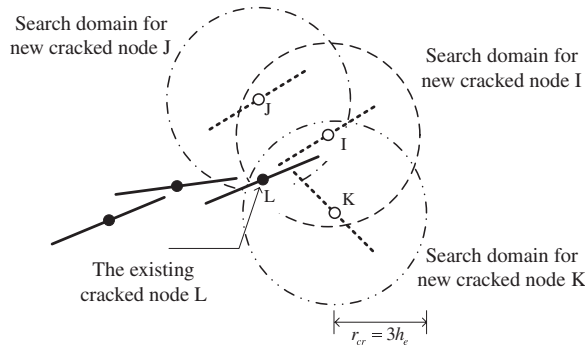


Figure 9. Schematic of crack propagation in general: nodes I , J , and K satisfy the fracture criterion at a given time step and the node L is the nearest existing cracked node.

phenomena such as the branching and the joining of cracks. Hence, the structure of these rules is somewhat delicate and must effectively deal with two issues:

- (1) distinguish whether a cracked node results from crack propagation or a nucleation process and
- (2) for the crack propagation case, it aims to prevent unrealistic parallel cracking patterns.

When a node satisfies the fracture criterion at a certain time step, we first distinguish whether the node is cracked due to crack *nucleation* or *propagation*. To determine this, we search the neighborhood within radius $r_{cr} = 3h_e$, where h_e is the element size, for any previously cracked nodes. If no previously cracked nodes are found within the search domain, the node is considered to crack due to *nucleation* and we inject a crack segment at the node without any further consideration.

However, if any previously cracked nodes are found within the search domain, we check whether the node satisfies the fracture *propagation* criterion and apply parallel cracking prevention laws. Consider the case shown in Figure 9 and suppose that in a given time step, nodes I , J , and K satisfy the fracture criterion and the node L is the nearest existing cracked node within the search domains of those nodes. We first set the parallel cracking prevention zone as shown in Figure 10. The parallel cracking prevention zone corresponding to node L is defined by

$$\left| \mathbf{n}_L \cdot \frac{\mathbf{X} - \mathbf{X}_L}{\|\mathbf{X} - \mathbf{X}_L\|} \right| < \cos\left(\frac{\pi}{2} - \alpha\right) \quad (50)$$

where α is the half-angle of the parallel cracking prevention zone: for the simulations in this study, we used $\alpha = 2\pi/9$.

For the case shown in Figure 10, we inject a crack segment at node I without checking for parallel cracking because the node I is not located within the parallel cracking prevention zone. However, for nodes J and K , which are located within the parallel cracking prevention zone, we compute the scalar product of the normals of the existing crack \mathbf{n}_L and the new cracks \mathbf{n}_J and \mathbf{n}_K , and then allow injection of a crack segment only when the scalar product is less than a specified value. In the case shown in Figure 10, we inject a crack segment only at node K because only node K satisfies

$$\mathbf{n}_L \cdot \mathbf{n}_K < \cos(\beta) \quad (51)$$

where β is a specified angle: we used $\beta = \pi/3$ for the simulations in this study.

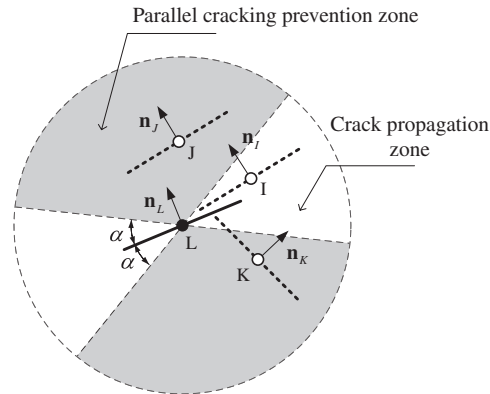


Figure 10. Schematic of parallel crack prevention zone.

7. NUMERICAL EXAMPLES

7.1. Edge-cracked plate under impulsive loading: Kalthoff problem

These simulations concern an experiment reported by Kalthoff and Winkler [47] in which a plate with two initial edge notches is impacted by a projectile, as shown in Figure 11(a). In the experiment [47], two different failures, shear and brittle failure modes, were observed by modifying the speed of the projectile. In this study, we consider only the brittle failure mode, in which the observed crack propagation angle was about 70° .

Taking advantage of the twofold symmetry of the experimental specimen, only the upper half of the plate is modeled as shown in Figure 11(b): at the bottom edge of the finite element model, $\bar{v}_y = 0$ and $\bar{t}_x = 0$ are applied as symmetric boundary conditions. We used 50×70 ($h_e = 1.0$ mm) and 24×36 ($h_e = 2.08$ mm) structured meshes, which were locally refined in the subdomain through which the crack is expected to propagate; the total number of elements for those models was 5438 and 2054, respectively. The initial impact velocity is applied on the left edge on the segment, $0 \leq y \leq 25$ mm. We assumed that the projectile has the same elastic impedance as the specimen; hence, we applied one half of the projectile speed, 16.5 m/s [48, 49]. The initial edge notch was modeled by including two lines of nodes separated by 300.0 μm . The material is a maraging steel 18Ni1900 [50] and its material properties are Young's modulus $E = 190$ GPa, density $\rho = 8000$ kg/m³, and Poisson's ratio $\nu = 0.30$. We used 0.5% maximum principal tensile strain as the fracture strain with fracture energy $G_f = 2.0 \times 10^4$ N/m.

A comparison of the final crack path with the two different meshes is shown in Figure 12. Both simulations are concluded at around 90 μs when the crack tip reaches the upper boundary. Both meshes show similar trajectories for the crack path. Until the mid-stage of crack growth, the cracks propagate with angles of about 60 and 55° for the fine and coarse mesh, respectively, except for a few vertical spurts, so that the average angle from the initial crack tip to the final crack tips is about 65° for both meshes. The overall crack paths are more jagged than that of continuous crack propagation methods [12, 14, 51, 52], but smoother than most interelement crack methods that have been reported.

A comparison of crack propagation speed with the conventional XFEM [12] is shown in Figure 13(a). The cracks start to propagate at around 30 μs for both meshes and then reach a

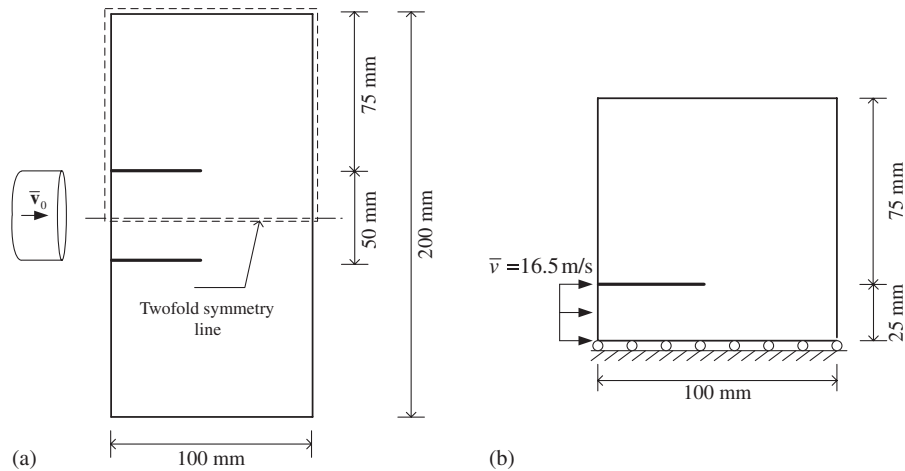


Figure 11. Problem set-up for edge-cracked plate under impact loading: (a) the original experimental set-up and (b) its numerical model.

constant speed around 2000 m/s, which is 71% of the Rayleigh wave speed $v_R = 2800$ m/s. Then, as the crack nears the upper boundary, the crack propagation speed slowly decreases. The computed crack speeds are almost identical with that of the conventional XFEM [12].

Time histories of the cohesive fracture energy for both meshes are shown in Figure 13(b). The cohesive fracture energy increases to around 1760 J and there is a little difference between the two meshes; hence, the results appear to have converged.

7.2. Crack branching problem

Crack branching due to a dynamic instability is a common phenomenon in dynamic fracture. Several experimental results with crack branching have been reported [53–55]; in these experiments, a crack starts growing at an initial notch and then the crack branches into at least two cracks: some of experiments show *more extensive and repetitive minor branches* [56].

However, only a few numerical results have been reported due to the difficulties of tracking complicated crack patterns; some examples can be found in [12, 14, 20]. To circumvent these difficulties, Belytschko *et al.* [12] and Song *et al.* [14] allowed the original crack to macroscopically branch only once. Although the Xu and Needleman method [20] can model multiple crack branches with the interelement cohesive crack model, the method exhibits mesh sensitivity; see Belytschko *et al.* [12] and Song *et al.* [29].

We consider a 100 mm \times 40 mm pre-notched specimen as shown in Figure 14. Tensile tractions, $\bar{\sigma} = 1$ MPa, are applied on both of the top and the bottom edges as a step function in time. The domain is discretized with 10 802 four-node quadrilateral elements; we used a locally refined mesh ($h_c^{\text{avg}} = 0.5$ mm) only where the crack is expected to propagate, i.e. ahead of the initial notch. The material properties are Young's modulus $E = 32$ GPa, density $\rho = 2450$ kg/m³, and Poisson's ratio $\nu = 0.20$. A cohesive law was used with a cohesive fracture energy $G_f = 3.0$ N/m.

The path of the crack at different times is shown in Figure 15(a)–(c). The crack starts to propagate at around 13.0 μ s and then branches into two major crack branches at around 30.2 μ s. Note that

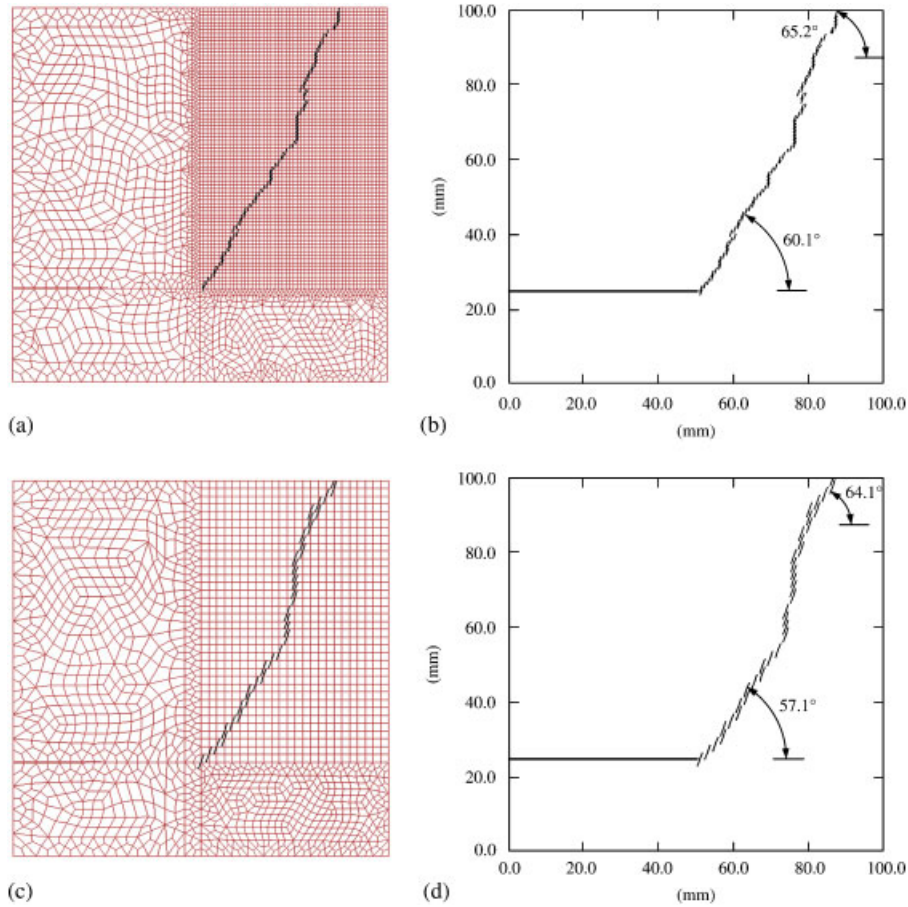


Figure 12. The crack paths with (a) and (b) locally refined 50×70 ($h_e = 1.0\text{mm}$) structured mesh and (c) and (d) locally refined 24×36 ($h_e = 2.08\text{mm}$) structured mesh.

in Figure 15(d), for better resolution of the crack opening, the final deformed configuration is magnified by a factor of 100. As can be seen from Figure 15, the major crack branches seen in the experiment [53] are reproduced quite well. In addition, some of the minor branches along the major crack branches are apparent as in Rabczuk and Belytschko [39].

Figure 16 shows the computed crack paths along with the experimental result of Ramulu and Kobayashi [53]. It is noteworthy that minor branches start to appear from the major crack prior to the major branching but only grow to small lengths; see Figure 16(b). This is completely missing in conventional XFEM calculations, which is a level-set-based discontinuity tracking method [12, 14]. However, the emergence of such minor crack branches before the major branching is only approximately reproduced by our method.

A comparison of the crack propagation speed with the results of conventional XFEM [12] is shown in Figure 17. Once the crack starts growing at around $13.0\mu\text{s}$, its speed quickly increases to its maximum speed 1500m/s until major crack branching occurs and then reaches a plateau around 1200m/s , which is 56% of Rayleigh wave speed $v_R = 2120\text{m/s}$.

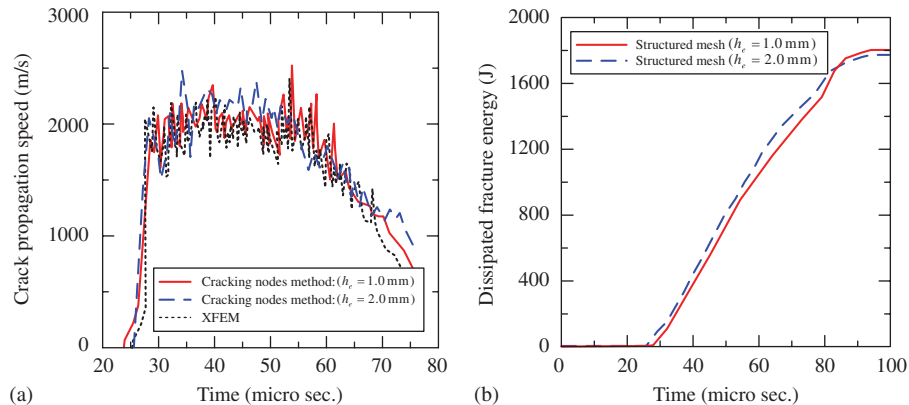


Figure 13. Time histories of the crack propagation speed and cohesive fracture energy: (a) crack propagation speeds compared with conventional XFEM [12] and (b) evolution of cohesive fracture energy.

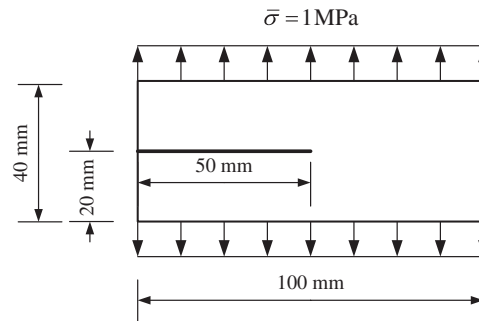


Figure 14. Initial set-up for crack branching problem.

The computed crack propagation speed is somewhat lower than that of conventional XFEM [12]. The discrepancy can be explained in terms of the dissipated fracture energy. The stored energy that drives crack propagation will decrease as a system dissipates more fracture energy to create new crack surfaces; hence, the crack propagation speed is also decreased [29, 57–59]. The cracking node method predicts several minor crack branches as shown in Figure 15, whereas the conventional XFEM [12] predicts only a major crack branch without minor branches. Therefore, the cracking node method dissipates more fracture energy than the conventional XFEM [12], which probably explains the lower crack propagation speed.

7.3. Fragmentation of thick cylinder problem

We consider fragmentation of a thick cylinder due to an applied impulsive internal pressure. The problem set-up is shown in Figure 18(a). The thickness of the cylinder is 70 mm and its inner and outer radii are 80 and 150 mm, respectively. An exponentially decaying internal pressure with respect to time, $p = p_0 e^{-t/t_0}$, is applied with initial pressure $p_0 = 400$ MPa and decay parameter $t_0 = 0.1$ ms; the time history of the applied internal pressure is shown in Figure 18(b). The material

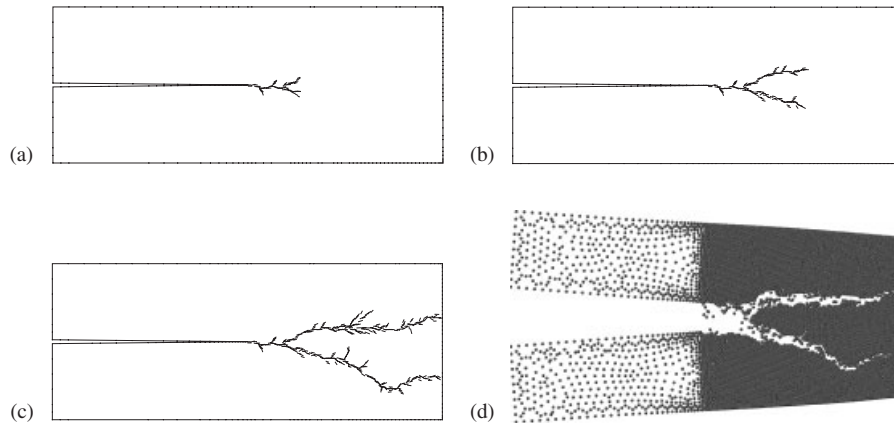


Figure 15. Crack branching at different time steps: (a) $t=33.13\ \mu\text{s}$; (b) $t=49.21\ \mu\text{s}$; (c) $t=60.3\ \mu\text{s}$; and (d) the final deformed configuration (magnified by a factor of 100).

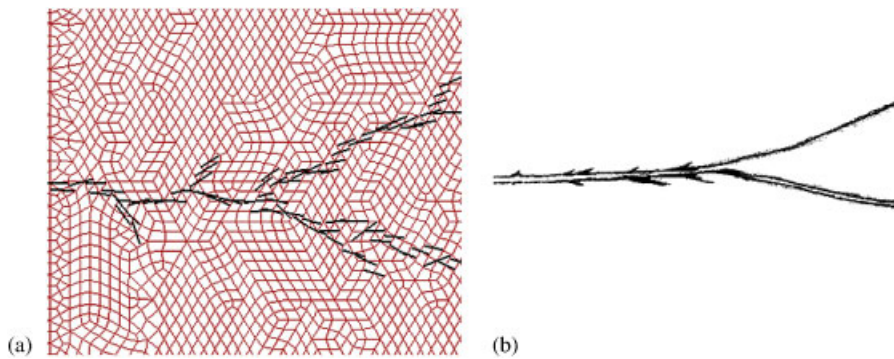


Figure 16. A comparison of crack branching phenomena: (a) zoom around major crack branches and (b) a sketch of the experiment reported by Ramulu and Kobayashi [53].

properties are: Young's modulus $E=210\text{GPa}$, density $\rho=7850\text{kg/m}^3$, and Poisson's ratio $\nu=0.30$. A $\pm 5\%$ perturbation in the elastic modulus was introduced to break the symmetry of the model. We used a maximum principal tensile strain criterion for fracture with a fracture strain of 0.5% ; the fracture energy is $G_f=2.0 \times 10^4\text{N/m}$. We discretized the cylinder with 75 202 ($h_e^{\text{avg}}=1.0\text{mm}$), 32 383 ($h_e^{\text{avg}}=1.5\text{mm}$), and 10 443 ($h_e^{\text{avg}}=3.0\text{mm}$) four-node quadrilateral unstructured elements.

Figure 19 shows the final crack patterns for the different mesh refinements. The number of fragments for the different refinements is given in Table I. Although arrested small cracks within fragments are more frequently observed with the finer mesh, the total number of fragments for the three meshes is almost identical. The overall fragmentation patterns are similar to that reported by Rabczuk and Belytschko [39] and Zhou and Molinari [31].

Figure 20 shows the fragmentation process at different times for the mesh discretized with 32 383 ($h_e^{\text{avg}}=1.5\text{mm}$) elements. The fragmentation process starts at around $40\ \mu\text{s}$ with a large number of

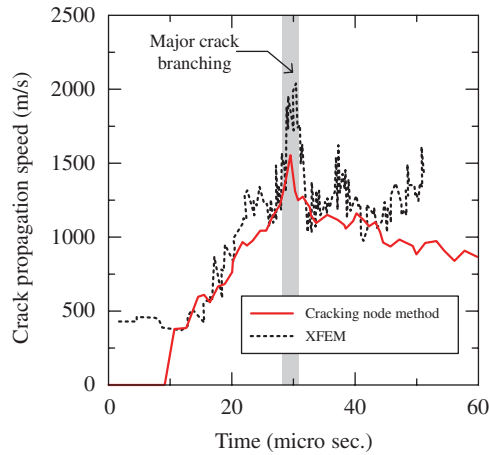


Figure 17. Crack propagation speed for the crack branching problem compared with the conventional XFEM [12].

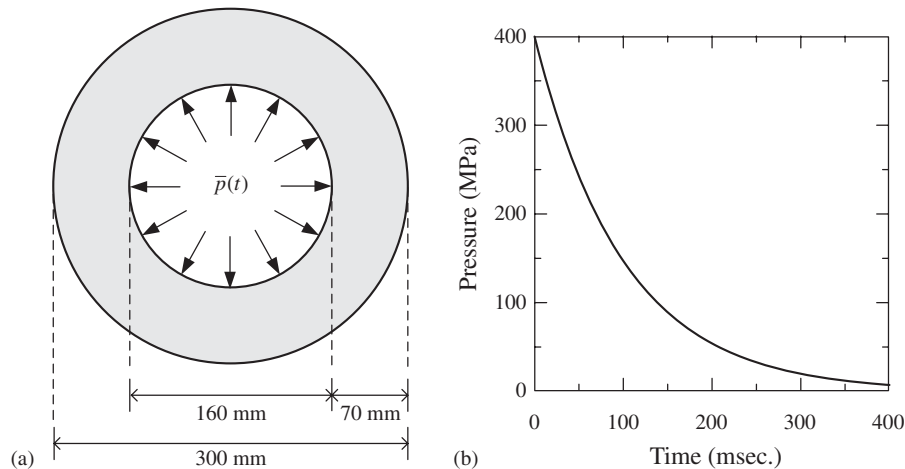


Figure 18. Problem set-up for fragmentation of thick cylinder under impulsive internal pressure.

small cracks along the inner surface. However, as the cracks grow, some of the initial cracks are arrested and then approximately only half of the cracks grow to the outer surface. The fragmentation process is finished at around $180\mu\text{s}$ and then the fragments move outward in the radial direction with no further crack initiation. The overall fragmentation processes with the different meshes are almost identical. The only difference is in the number of initial cracks and arrested cracks; fine meshes exhibit more initial cracks.

Time histories of the cohesive fracture energy for different mesh refinements are shown in Figure 21. At the beginning of the fragmentation, the fracture energy is dissipated very quickly until about $60\mu\text{s}$ due to a large number of initial cracks. However, after some of the cracks are

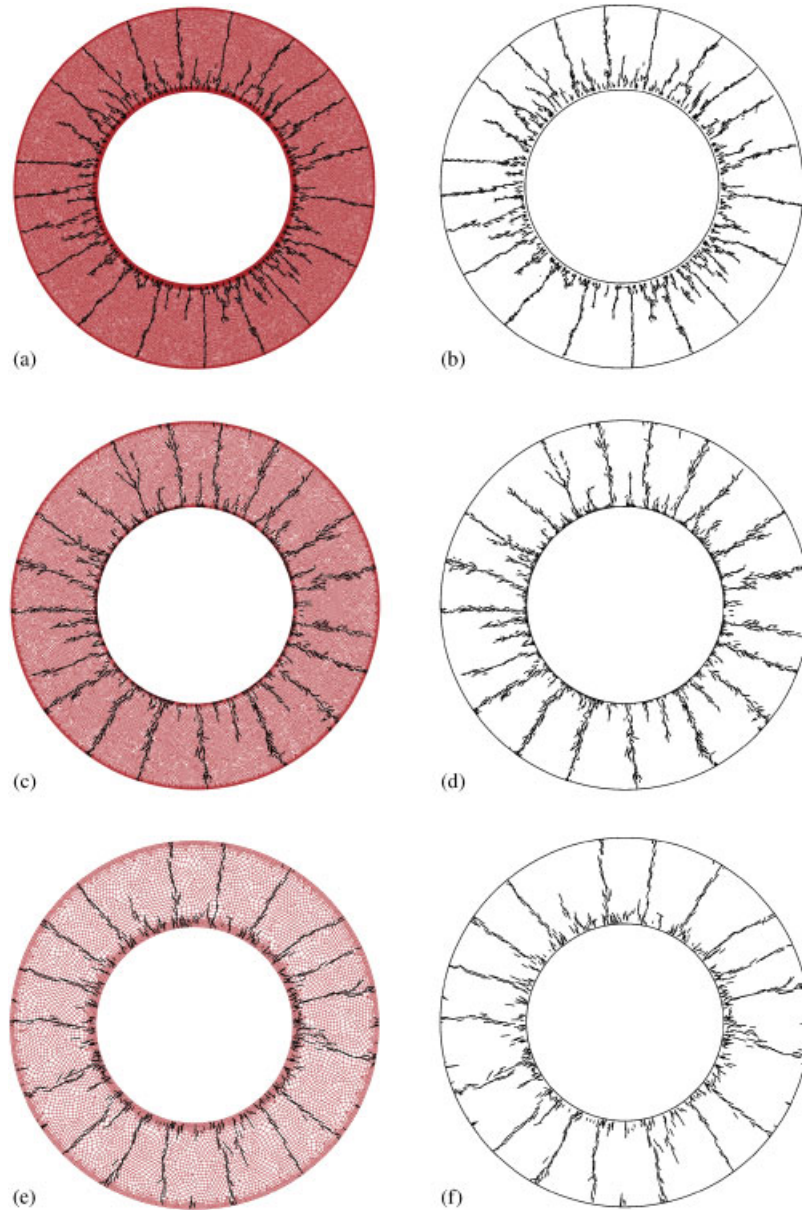


Figure 19. The crack paths for different unstructured mesh refinements with (a) and (b) 75 202 ($h_e^{\text{avg}} = 1.0$ mm) elements, (c) and (d) 32 383 ($h_e^{\text{avg}} = 1.5$ mm) elements, and (e) and (f) 10 443 ($h_e^{\text{avg}} = 3.0$ mm) elements.

arrested, the rate of fracture energy dissipation decreases. The total dissipated fracture energies for different meshes agree quite closely; hence, there is little mesh dependence even beyond the coarsest mesh.

Table I. The number of fragments for the cylinder with the different mesh refinements.

Number of element	Number of fragments
75 202 ($h_e^{\text{avg}} = 1.0 \text{ mm}$)	20
32 383 ($h_e^{\text{avg}} = 1.5 \text{ mm}$)	19
10 443 ($h_e^{\text{avg}} = 3.0 \text{ mm}$)	18

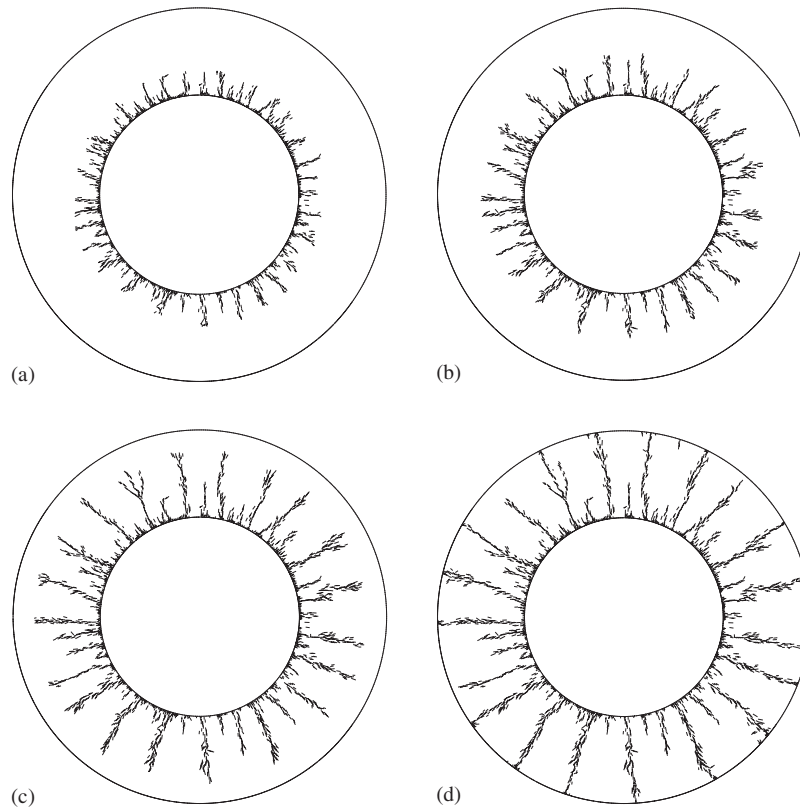


Figure 20. The formation of fragments with 32 383 ($h_e^{\text{avg}} = 1.5 \text{ mm}$) elements mesh at (a) 44.2 μs , (b) 63.5 μs , (c) 120.1 μs , and (d) 190.9 μs .

8. CONCLUSIONS

A new method for modeling of crack growth by a set of discrete crack segments has been proposed. In this method, the crack segments are restricted to pass through the nodes of the finite element mesh and span only two adjacent elements. Each of the crack segments normals is independently determined by the material failure laws; in the computations here, a maximum tensile principal strain criterion was employed.

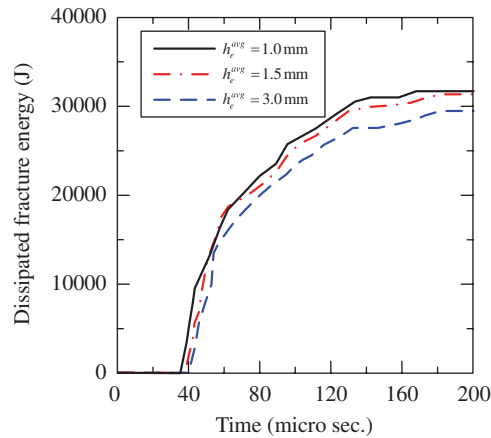


Figure 21. Time histories of the cohesive fracture energy.

The principal attractions of this method are its simplicity and robustness:

- (1) an explicit representation of the topology of the actual crack path is unnecessary because the actual crack path is naturally approximated with contiguous crack segments,
- (2) complicated dynamic fracture behaviors such as crack branching and fragmentation are easily handled with the method, and
- (3) only minor changes are needed to implement the method in a typical explicit finite element code.

However, the use of discrete crack segments also limits the accuracy of the method somewhat and results in some drawbacks. The major drawback is that the method needs to introduce certain discretization rules that are difficult to substantiate mathematically. The most noteworthy of these are the rules on spurious parallel node cracking. Without such rules, extensive patterns of spurious parallel cracks can be developed and it provides nonphysical results. However, as mentioned in the paper, such rules can be justified by the inability of any mesh to resolve such patterns of cracking.

The accuracy and effectiveness of the method have been demonstrated by comparisons with previously reported experiments [47, 53] and computational results [12]. Overall crack paths and crack propagation speeds converge quite rapidly with mesh refinement and agree well with the reference solutions. The fracture energies also converge rapidly and show almost no mesh dependence.

ACKNOWLEDGEMENTS

The support of the Office of Naval Research under Grant N00014-06-1-0380 is gratefully acknowledged.

REFERENCES

1. Swenson DV, Ingraffea AR. Modelling mixed-mode dynamic crack propagation using finite elements: theory and applications. *Computational Mechanics* 1988; **3**:187–192.
2. Martha LF, Wawrzynek PA, Ingraffea AR. Arbitrary crack representation using solid modeling. *Engineering with Computers* 1993; **9**:63–82.
3. Belytschko T, Black T. Elastic crack growth in finite elements with minimal remeshing. *International Journal for Numerical Methods in Engineering* 1999; **45**(5):601–620.

4. Moës N, Dolbow J, Belytschko T. A finite element method for crack growth without remeshing. *International Journal for Numerical Methods in Engineering* 1999; **46**(1):131–150.
5. Babuška I, Melenk JM. The partition of unity method. *International Journal for Numerical Methods in Engineering* 1997; **40**(4):727–758.
6. Stolarska M, Chopp DL, Moës N, Belytschko T. Modeling crack growth by level sets in the extended finite element method. *International Journal for Numerical Methods in Engineering* 2001; **51**(8):943–960.
7. Belytschko T, Moës N, Usui S, Parimi C. Arbitrary discontinuities in finite elements. *International Journal for Numerical Methods in Engineering* 2001; **50**(4):993–1013.
8. Ventura G, Xu JX, Belytschko T. A vector level set method and new discontinuity approximations for crack growth by EFG. *International Journal for Numerical Methods in Engineering* 2002; **54**:923–944.
9. Ventura G, Budyn E, Belytschko T. Vector level sets for description of propagating cracks in finite elements. *International Journal for Numerical Methods in Engineering* 2003; **58**:1571–1592.
10. Prabel B, Combescure A, Gravouil A, Marie S. Level set X-FEM non-matching meshes: application to dynamic crack propagation in elastic–plastic media. *International Journal for Numerical Methods in Engineering* 2007; **69**:1553–1569.
11. Areias PMA, Belytschko T. Analysis of three-dimensional crack initiation and propagation using the extended finite element method. *International Journal for Numerical Methods in Engineering* 2005; **63**:760–788.
12. Belytschko T, Chen H, Xu J, Zi G. Dynamic crack propagation based on loss of hyperbolicity with a new discontinuous enrichment. *International Journal for Numerical Methods in Engineering* 2003; **58**:1873–1905.
13. Zi G, Song JH, Lee SH, Budyn E, Belytschko T. A new method for multiple cracks and its application to fatigue crack growth. *Modeling and Simulations in Materials Science and Engineering* 2004; **12**:901–915.
14. Song JH, Areias PMA, Belytschko T. A method for dynamic crack and shear band propagation with phantom nodes. *International Journal for Numerical Methods in Engineering* 2006; **67**:868–893.
15. Areias PMA, Song JH, Belytschko T. A finite-strain quadrilateral shell element based on discrete Kirchhoff–Love constraints. *International Journal for Numerical Methods in Engineering* 2005; **64**:1166–1206.
16. Areias PMA, Song JH, Belytschko T. Analysis of fracture in thin shells by overlapping paired elements. *Computer Methods in Applied Mechanics and Engineering* 2006; **195**:5343–5360.
17. Song JH, Belytschko T. Dynamic fracture of shells subjected to impulsive loads. *Journal of Applied Mechanics* 2008, in review.
18. Fish J. The *s*-version of the finite element method. *Computers and Structures* 1992; **43**(3):539–547.
19. Belytschko T, Chiapetta RL, Bartel HD. Efficient large-scale nonlinear transient analysis finite-elements. *International Journal for Numerical Methods in Engineering* 1976; **10**:579–596.
20. Xu X-P, Needleman A. Numerical simulation of fast crack growth in brittle solids. *Journal of the Mechanics and Physics of Solids* 1994; **42**(9):1397–1434.
21. Camacho G, Ortiz M. Computational modelling of impact damage in brittle materials. *International Journal of Solids and Structures* 1996; **33**:2899–2938.
22. Belytschko T, Fish J, Engelmann BE. A finite element with embedded localization zones. *Computer Methods in Applied Mechanics and Engineering* 1988; **70**:59–89.
23. Strouboulis T, Babuška I, Coops K. The design and analysis of generalized finite element method. *Computer Methods in Applied Mechanics and Engineering* 2000; **181**:43–69.
24. Duarte CA, Oden JT, Babuška I. Generalized finite element methods for three-dimensional structural mechanics problems. *Computers and Structures* 2000; **77**:215–232.
25. Duarte CA, Reno LG, Simone A. High-order generalized FEM for through-the-thickness branched cracks. *International Journal for Numerical Methods in Engineering* 2007; **72**:325–351.
26. Ortiz M, Pandolfi A. Finite-deformation irreversible cohesive elements for three-dimensional crack-propagation analysis. *International Journal for Numerical Methods in Engineering* 1999; **44**:1267–1282.
27. Papoulia KD, Sam CH, Vavasis SA. Time continuity in cohesive finite element modeling. *International Journal for Numerical Methods in Engineering* 2003; **58**:679–701.
28. Papoulia KD, Vavasis SA, Ganguly P. Spatial convergence of crack nucleation using a cohesive finite-element model on a pinwheel-based mesh. *International Journal for Numerical Methods in Engineering* 2006; **67**:1–16.
29. Song JH, Wang HW, Belytschko T. A comparative study on finite element methods for dynamic fracture. *Computational Mechanics*. DOI: 10.1007/s00466-007-0210-x.
30. Zavattieri PD, Espinosa HD. Grain level analysis of crack initiation and propagation in brittle materials. *Acta Materialia* 2001; **49**:4291–4311.
31. Zhou F, Molinari JF. Dynamic crack propagation with cohesive elements: a methodology to address mesh dependency. *International Journal for Numerical Methods in Engineering* 2004; **59**:1–24.

32. Dvorkin EN, Cuitino AM, Gioia G. Finite elements with displacement interpolated embedded localization lines insensitive to mesh size and distortions. *International Journal for Numerical Methods in Engineering* 1990; **30**:541–564.
33. Simo JC, Oliver J, Armero F. An analysis of strong discontinuities induced by strain-softening in rate-independent inelastic solids. *International Journal for Numerical Methods in Engineering* 1993; **12**:277–296.
34. Armero F, Garikipati K. An analysis of strong discontinuities in multiplicative finite strain plasticity and their relation with the numerical simulation of strain localization in solids. *International Journal of Solids and Structures* 1996; **33**:2863–2885.
35. Jirásek M. Comparative study on finite elements with embedded discontinuities. *Computer Methods in Applied Mechanics and Engineering* 2000; **188**:307–330.
36. Fan R, Fish J. The rs-method for material failure simulations. *International Journal for Numerical Methods in Engineering* 2008; **73**:1607–1623.
37. Remmers JJC, de Borst R, Needleman A. A cohesive segments method for the simulation of crack growth. *Computational Mechanics* 2003; **31**:69–77.
38. de Borst R, Remmers JJC, Needleman A. Mesh-independent discrete numerical representations of cohesive-zone models. *Engineering Fracture Mechanics* 2006; **73**:160–177.
39. Rabczuk T, Belytschko T. Cracking particles: a simplified meshfree method for arbitrary evolving cracks. *International Journal for Numerical Methods in Engineering* 2004; **61**:2316–2343.
40. Rabczuk T, Areias PMA, Belytschko T. A simplified meshfree method for shear bands with cohesive surfaces. *International Journal for Numerical Methods in Engineering* 2007; **69**:993–1021.
41. Rabczuk T, Samaniego E. Discontinuous modelling of shear bands using adaptive meshfree methods. *Computer Methods in Applied Mechanics and Engineering* 2008; **107**:641–658.
42. Belytschko T, Liu WK, Moran B. *Nonlinear Finite Elements for Continua and Structures*. Wiley: New York, 2000.
43. Flanagan DP, Belytschko T. A uniform strain hexahedron and quadrilateral with orthogonal hourglass control. *International Journal for Numerical Methods in Engineering* 1981; **17**:679–706.
44. Daniel WJT, Belytschko T. Suppression of spurious intermediate frequency modes in under-integrated elements by combined stiffness/viscous stabilization. *International Journal for Numerical Methods in Engineering* 2005; **64**:335–353.
45. Menouillard T, Réthoré J, Combescure A, Bung H. Efficient explicit time stepping for the extended finite element method. *International Journal for Numerical Methods in Engineering* 2006; **68**:911–939.
46. Menouillard T, Réthoré J, Moës N, Combescure A, Bung H. Mass lumping strategies for X-FEM explicit dynamics: application to crack propagation. *International Journal for Numerical Methods in Engineering* 2007; DOI: 10.1002/nme.2180.
47. Kalthoff JF, Winkler S. Failure mode transition at high rates of shear loading. *International Conference on Impact Loading and Dynamic Behavior of Materials* 1987; **1**:185–195.
48. Lee YJ, Freund LB. Fracture initiation due to asymmetric impact loading of an edge cracked plate. *Journal of Applied Mechanics (ASME)* 1990; **57**:104–111.
49. Kalthoff JF. Modes of dynamic shear failure in solids. *International Journal of Fracture* 2000; **101**:1–31.
50. Decker RF. *Source Book on Maraging Steels*. American Society for Metals: Cleveland, OH, 1979.
51. Belytschko T, Tabbara M. Dynamic fracture using element-free Galerkin methods. *International Journal for Numerical Methods in Engineering* 1996; **39**:923–938.
52. Réthoré J, Gravouil A, Combescure A. An energy-conserving scheme for dynamic crack growth using the extended finite element method. *International Journal for Numerical Methods in Engineering* 2005; **63**:631–659.
53. Ramulu M, Kobayashi AS. Mechanics of crack curving and branching—a dynamic fracture analysis. *International Journal of Fracture* 1985; **27**:187–201.
54. Satoh H. On the crack propagation in brittle materials. *Ph.D. Thesis*, University of Tokyo, Japan, 1996.
55. Ravi-Chandar K. Dynamic fracture of nominally brittle materials. *International Journal of Fracture* 1998; **90**:83–102.
56. Sharon E, Fineberg J. Microbranching instability and the dynamic fracture of brittle materials. *Physical Review B* 1996; **54**(10):7128–7139.
57. Sharon E, Gross SP, Fineberg J. Energy dissipation in dynamic fracture. *Physical Review Letters* 1996; **76**(12):2117–2120.
58. Sharon E, Fineberg J. Confirming the continuum theory of dynamic brittle fracture for fast cracks. *Letters to Nature* 1999; **397**:333–335.
59. Rabczuk T, Song JH, Belytschko T. Simulations of instability in dynamic fracture by the cracking particles method. *Engineering Fracture Mechanics* 2008, accepted.